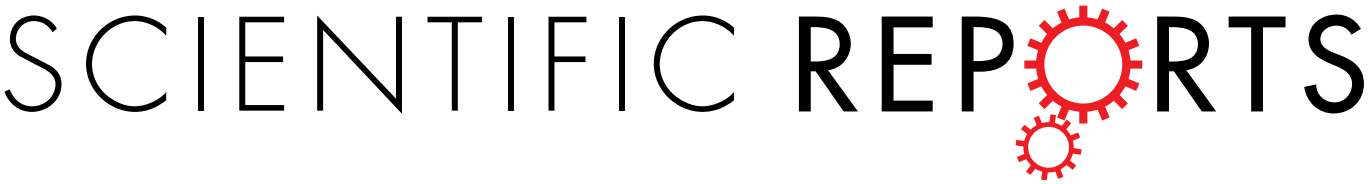

OPEN

# Sensing and Impedance Characteristics of $YbTaO_4$ Sensing Membranes

Received: 15 January 2018
Accepted: 9 August 2018
Published online: 27 August 2018

Tung-Ming Pan[1,2], Yu-Shu Huang[1] & Jim-Long Her[3]

**In this study we developed ytterbium tantalum oxide ($YbTaO_4$) sensing membranes for use in electrolyte–insulator–semiconductor (EIS) pH sensors. The influence of rapid thermal annealing (RTA) treatment on the sensing and impedance properties of the $YbTaO_4$ sensing membranes deposited through reactive co-sputtering onto Si substrates was explored. X-ray diffraction, atomic force microscopy, and X-ray photoelectron spectroscopy revealed the structural, morphological, and chemical features, respectively, of these $YbTaO_4$ films annealed at 700, 800 and 900 °C. The $YbTaO_4$ EIS device annealed at the 800 °C exhibited a super-Nernstian response of 71.17 mV/pH within the pH range of 2–12. It also showed the lowest hysteresis voltage (< 1 mV) and the lowest drift rate (0.22 mV/h) among the tested systems. Presumably, the optimal annealing temperature improved the stoichiometry of $YbTaO_4$ film and increased its (−131)-oriented nanograin size. Moreover, the impedance properties of $YbTaO_4$ EIS sensors were investigated by using the capacitance–voltage method. The resistance and capacitance of $YbTaO_4$ sensing films annealed at three various temperatures were evaluated by using different frequency ranges in accumulation, depletion, and inversion regions. The semicircle diameter of the $YbTaO_4$ EIS sensor became smaller, due to a gradual decrease in the bulk resistance of the EIS device, as the RTA temperature was increased.**

An ion-sensitive field-effect-transistor (ISFET) device was first developed by Bergveld in 1970 as a replacement for a fragile glass electrode[1]. Over the past four decades, research on various kinds of ISFET-based biosensors, for example glucose, urea, protein, DNA hybridization, and DNA methylation detection[2–7], has been conducted because they have the advantages of fast response, small size, and low cost. In general, the gate electrode of a conventional metal-oxide-semiconductor field-effect transistor (MOSFET) is replaced by a chemically sensitive oxide layer, an electrolyte, and a reference electrode to become an ISFET device. An electrolyte-insulator-semiconductor (EIS) capacitor has a simple structure and easy fabrication with respect to an ISFET device. The surface potential of such an ISFET is modulated by the change in the charges at the interface between the oxide layer and electrolyte, thus leading to the shift of the threshold voltage and the variation of the drain-source current. As a result, quality and chemical stability of the sensing film play a key role in the applications of an ISFET or EIS device. The most widely used sensitive oxide film is $SiO_2$ in ISFETs, but its application is severely limited by its poor sensitivity[8]. Therefore, $Si_3N_4$, $Al_2O_3$, $Ta_2O_5$, $TiO_2$, $ZrO_2$, and $HfO_2$ films were investigated as alternative sensitive oxides in ISFETs or EISs to improve their sensitivities[9–12]. However, the pH sensitivity of the traditional ISFET or EIS sensors could not exceed the Nernstian limit (59.18 mV/pH at 25 °C) because of intrinsic properties of these metal oxide films. In addition, there are some materials related problems with silicide at the interface of oxide film/Si substrate after thermal treatment and dangling bonds on the sensing film during the thin-film deposition to impact their sensing performance[13,14].

In search of the low defect density and high thermal stability in high dielectric constant (κ) metal oxide films, rare-earth (RE) oxide thin films have been studied for use as a replacement MOSFET gate dielectric due to their high κ values, large bandgap energies, good thermodynamic properties, high resistivities, and high conduction-band offsets[15,16]. Of these RE oxides, ytterbium oxide ($Yb_2O_3$) thin film turns out to be a potential gate oxide because of its novel properties, including excellent thermal and chemical stability, large bandgap (~5 eV), and high κ (~15), in which the κ values depend on deposition processing[17,18]. Nevertheless, due to the highly

[1]Department of Electronics Engineering, Chang Gung University, Taoyuan, 33302, Taiwan. [2]Division of Urology, Chang Gung Memorial Hospital, Taoyuan, 33305, Taiwan. [3]Division of Natural Science, Center for General Education, Chang Gung University, Taoyuan, 33302, Taiwan. Correspondence and requests for materials should be addressed to T.-M.P. (email: tmpan@mail.cgu.edu.tw)

hygroscopic nature, there is a need to develop the fabrication of stable RE oxide film, suppressing the formation of a hydroxide layer on the film because of the presence of oxygen vacancies[19]. The formation of oxygen vacancies can contribute to the occurrence of a sufficient atomic reorganization in the film structure. In order to solve the aforementioned shortcoming, in an effort to remove the oxygen vacancies in the RE oxide film, the addition of Ti or $TiO_2$ into the film could be reduced the moisture absorption of RE oxides, thereby improving the structural and electrical properties[20,21]. Recently, our group previously demonstrated the structural and sensing characteristics of $Yb_2Ti_2O_7$ sensing films in an EIS sensor[22], in contrast, the resistance to the level of moisture absorption for the incorporation of Ta into the $Yb_2O_3$ film after post-annealing treatment to eliminate the oxygen vacancies is still unclear. The aim of this paper is to explore the effect of post-annealing treatment on the structural, sensing, and impedance characteristics of ytterbium tantalum oxide ($YbTaO_4$) sensing films deposited on Si substrates through reactive rf co-sputtering. X-ray diffraction (XRD), atomic force microscope (AFM), and X-ray photoelectron spectroscopy (XPS) were employed to examine the film structures, surface morphologies, and chemical compositions of $YbTaO_4$ films annealed at three different temperatures (700, 800 and 900 °C), respectively. In addition, structural characteristics of the $YbTaO_4$ films are correlated to sensing and impedance properties of the EIS sensors after annealing at three temperatures. In this study, the $YbTiO_4$ membrane after RTA at 800 °C showed a higher pH sensitivity (71.17 mV/pH), a smaller hysteresis voltage (<1 mV) and a lower drift rate (0.22 mV/h), compared with other RTA temperatures.

## Methods

**Fabrication.** Prior to the deposition of sensing film, the Si substrate was cleaned and hydrogen-terminated by using diluted HF. The $YbTa_xO_y$ thin films were grown on p-Si (100) substrates with a resistivity of 5–10 Ω-cm by rf co-sputtering using from metal Yb and Ta as target materials in a mixture of $Ar/O_2$ (5 sccm/20 sccm). The plasma power of Yb and Ta targets was 100 W. The chamber pressure was $1 \times 10^{-3}$ Torr during the growth process and the substrate temperature was 27 °C. The growth rate and physical thickness of the $YbTa_xO_y$ film were ~2 nm/min and ~60 nm, respectively. Subsequently, the samples were annealed at three various temperatures (700, 800 and 900 °C) by rapid thermal annealing (RTA) in oxygen ($O_2$) ambient for 30 s to form an $YbTaO_4$ compound. Next, the back-side oxide of Si wafer was etched by buffer oxide etchant (BOE) solution and Al (400 nm thick) as a back-side electrode was deposited by thermal evaporation to achieve good electrical contact. The sensing area of 3.14 $mm^2$ was defined by a robotic dispensing system using an adhesive silicone gel (S181) as an isolating layer. The EIS device was mounted on the Cu-coated printed circuit board (PCB) with an Al back-side contact through Ag paste. Finally, the non-sensing region of the EIS sensor was covered with epoxy.

**Characterization.** The orientation and phase of these films were investigated by XRD (Bruker D8 discover diffractometer) in a scan range of $2\theta = 20°–60°$ using a step time of 1 s and a step size of 0.05°. The Cu $K_\alpha$ radiation ($\lambda = 1.5406$ Å) was run under a voltage of 40 kV and a current of 20 mA. A tapping mode AFM (NT-MDT Solver P47) was employed to explore the surface topography and determine the surface roughness (root-mean-square, $R_{rms}$) of the $YbTaO_4$ films annealed at three temperatures. The $R_{rms}$ roughness of these samples was estimated in scanning areas of $3 \times 3$ $\mu m^2$. The film composition of $YbTaO_4$ films was analyzed using XPS (Thermo VG Scientific Microlab 350 system) with a monochromatic Al $K_\alpha$ source (1486.7 eV). The binding energy scale of each element was calibrated by setting the main hydrocarbon peak at a binding energy of 285 eV (C 1 s).

**Measurement.** The pH sensitivity, hysteresis voltage, and drift rate of the $YbTaO_4$ EIS devices were evaluated by capacitance–voltage (C–V) curves. The C–V measurements for different pH buffer solutions (Merck Inc.) were performed using inductance–capacitance–resistance (LCR) meter (Agilent 4284 A), operated at 500 Hz with an applied ac voltage of 10 mV. The Ag/AgCl electrode (commercial liquid-junction electrode) electrode as a reference electrode was used. The impedance measurement of EIS devices was performed by a combination of Agilent 4284 A and 4285 A LCR meters. To achieve the steady results, all samples were kept in reverse osmosis (RO) water for 24 h before measurement. The sensing membrane was washed with deionized water before transferring to subsequent pH solution. In order to prevent light and noise interference, all the measurements were performed in a dark box. Three devices on each sample were repeated at least three times to measure sensing performance of the $YbTaO_4$ EIS sensors.

## Results and Discussion

**Structural properties of $YbTaO_4$ sensing films.** The XRD patterns of all $YbTaO_4$ films deposited on a Si substrate after RTA at different temperatures (700–900 °C) in $O_2$ ambient were presented in Fig. 1. The $YbTaO_4$ films after RTA at three temperatures have a monoclinic structure. The $YbTaO_4$ diffraction peaks were recorded at (310) and (−131) peaks for the film annealed at 700 °C. Apart from the increment in the intensity of the existing $YbTaO_4$ peaks, an additional $YbTaO_4$ (011), (−111), (111), (020), (200), (120), (022), and (202) peaks (JCPDS: 00-024-1416) were detected when the annealing temperature was raised up to 800 °C, suggesting a polycrystalline structure. These peaks became more noticeable as the annealing temperature increased. By further increasing the annealing temperature to 900 °C, the increment in the intensity of $YbTaO_4$ (−111), (111), (020), (200), and (120) peaks was observed. Overall, as the RTA temperature increased from 700 °C to 800 °C, the intensity of the $YbTaO_4$ (−131) peak increased. This condition may indicate the reduction of oxygen vacancies present in the film due to the highest stability offered by (−131)-oriented $YbTaO_4$. The crystallite size (or grain size) of the $YbTaO_4$ film after three RTA temperatures is determined by using the Scherrer's equation for the main diffraction peak[23]. The average grain size was calculated to be 0.12, 0.21, and 0.24 nm for the sample annealed at 700, 800 and 900 °C, respectively. Moreover, the crystallite size of the (−131) peak for the $YbTaO_4$ film annealed at 700, 800 and 900 °C was 0.12, 0.35 and 0. 19 nm, respectively.

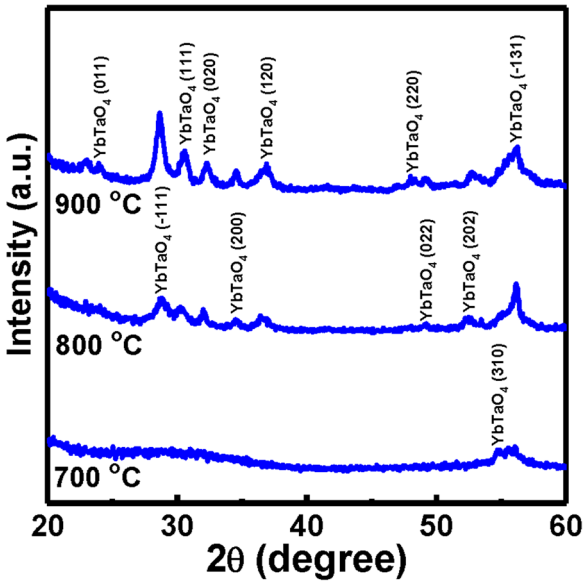


**Figure 1.** XRD patterns of $YbTaO_4$ films annealed at three different RTA temperatures.

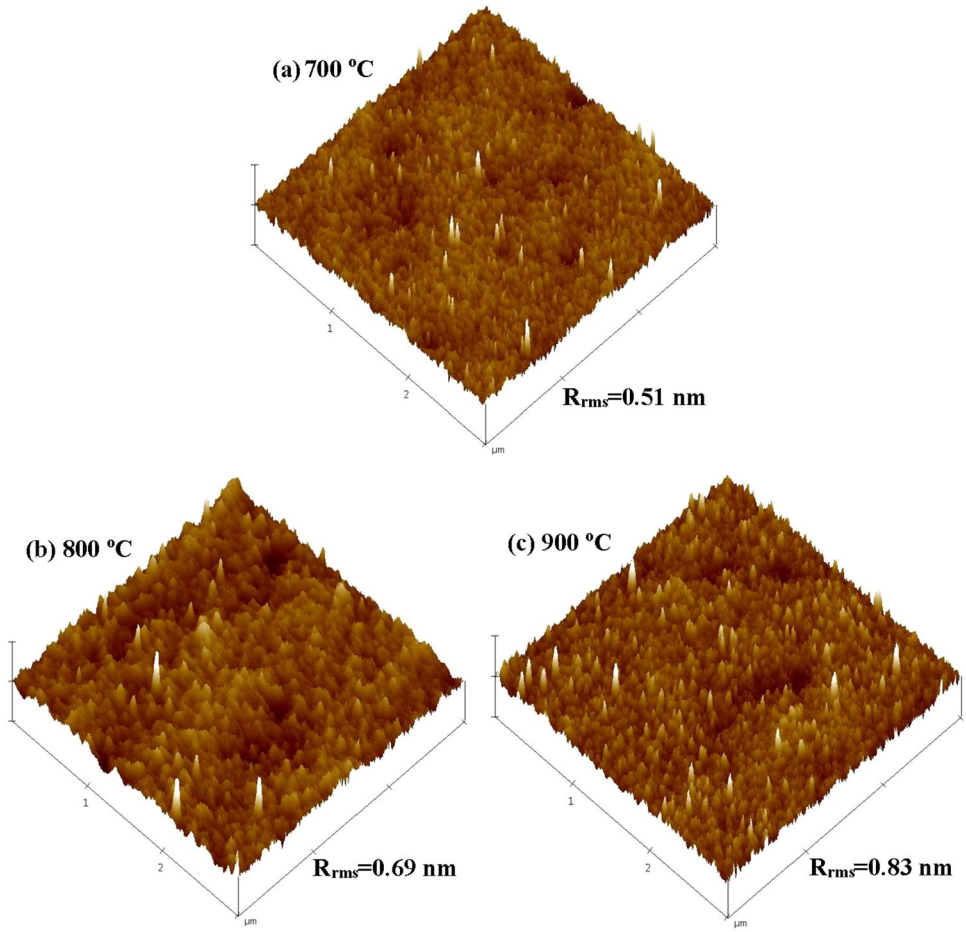


**Figure 2.** AFM images of $YbTaO_4$ films annealed at three RTA temperatures: (**a**) 700 °C, (**b**) 800 °C and (**c**) 900 °C.

The surface morphology of $YbTaO_4$ thin films deposited on a Si substrate was evaluated by AFM to examine the effect of RTA temperatures. Figure 2 depicts AFM 3-D surface topographies and $R_{rms}$ roughnesses of the $YbTaO_4$ films annealed at various temperatures. In general, the sample is uniform and smooth without defects,

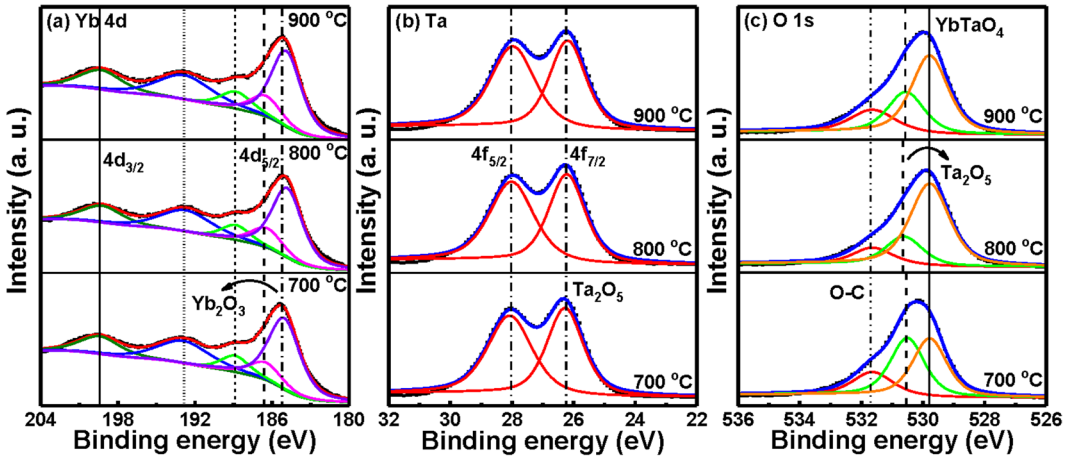


**Figure 3.** XPS spectra displaying the (**a**) Yb 3d, (**b**) Ta 4 f, and (**c**) O 1 s energy levels in $YbTaO_4$ films annealed at three RTA temperatures.

such as a crack or void. It can be observed in Fig. 2 that bubblelike grains were developed for all samples. When the film was annealed at 900 °C, more bubblelike grains were formed in contrast to the film annealed at 800 and 700 °C. The $R_{rms}$ roughness of the $YbTaO_4$ films annealed at 700, 800 and 900 °C was 0.51, 0.69 and 0.83 nm, respectively. The $R_{rms}$ roughness of the sample is in the increasing trend as the RTA temperature increases. The reason of increase of surface roughness might be attributed to the growth of grain size due to the formation of grain agglomerations in the film after annealing at high temperature in oxygen gas. This result indicates that the grain size increases with increasing RTA temperature, as expected, leading to the enhanced crystallinity and the sharpened diffraction peaks. Therefore, the obtained $R_{rms}$ roughness from AFM matches with the XRD results. Hence, more $YbTaO_4$ was formed, and a noticeable change in the surface morphology was observed for the sample annealed at 900 °C.

The valence states of Yb, Ta, and O elements in a $YbTaO_4$ layer were analyzed by XPS with $Ar^+$ ion etching. The 30 s etching process was conducted to remove the surface contamination. The obtained Yb 3d, Ta 4 f and O 1 s spectra of the $YbTaO_4$ films after RTA at three temperatures were shown in Fig. 3. After the subtraction of Shirley-type backgrounds, the raw data were all fitted by Gaussian-Lorentzian line shapes. To determine the valence state of Yb in the films annealed at various temperatures, we investigated the XPS spectra of the Yb 4d level in the $YbTaO_4$. The ytterbium compounds have two valence states. The filled 4 f shell of divalent ytterbium ($Yb^{2+}$) in the 4d spectrum is a doublet with a peak area ratio of 3:2, while partially filled 4 f shell of trivalent ytterbium ($Yb^{3+}$) is a multiplet[24]. The electronic structure of the Yb 4d multiplet peaks in these films is in good agreement with multiplet splitting in the Yb 4d spectrum of $Yb_2O_3$, which is different from the 4d doublet of $Yb^{2+}$. There are two main Yb $4d_{3/2}$ and $4d_{5/2}$ peaks centered at $199.5 \pm 0.1$ eV and $185.3 \pm 0.1$ eV, respectively, which are consistent with the binding energy of Yb 4d for $Yb_2O_3$ ref.[25]. The Yb $4d_{5/2}$ peak of the film annealed at 800 and 900 °C was slightly shifted toward a higher binding energy, suggesting the incorporation of more Ta atom into the $Yb_2O_3$ film forming a $YbTaO_4$ compound. Figure 3(b) shows the double peak features in the Ta 4f XPS spectra for $YbTaO_4$ films annealed at three temperatures. The Ta $4f_{5/2}$ and $4f_{7/2}$ peaks located at binding energies of 28.1 and 26.2 eV, respectively, are assigned to pure $Ta_2O_5$ film[26]. The spin-orbit splitting energy of $Ta_2O_5$ film was 1.9 eV from Ta $4f_{5/2}$ to Ta $4f_{7/2}$ peak. The deconvolution results of these $YbTaO_4$ films demonstrated a perfect fit for Ta $4f_{5/2}$ and $4f_{7/2}$ peaks located at two $28 \pm 0.1$ and $26.1 \pm 0.1$ eV and splitting energy of ~1.9 eV, which are in good agreement with the reported values for $Ta_2O_5$ ref.[26] indicating that the Ta exhibits the highest oxidation state. These sensing films consist of tantalum suboxides ($Ta_2O_5$) with no $TaO_x$ content. The splitting energy of about 1.9 eV can consider strong binding interaction between the tantalum and the oxygen atoms. The reaction of $Ta_2O_5$ with $Yb_2O_3$ can form a $YbTa_xO_y$ compound. The O 1 s XPS spectra of the $YbTaO_4$ films after RTA at different temperatures were deconvoluted with Gaussian-Lorentzian curve fitting after the Shirley background, as shown in Fig. 3(c). The fitting results depicted three peaks located at 531.6, ~530.5, and 529.8 eV. The high binding-energy peak of 531.6 eV corresponds to the surface contamination is caused by adsorption of atmospheric carbon-containing species. The median binding-energy peak of 530.5 eV can be related to the $O^{2-}$ species occurring in $Ta_2O_5$[26]. The low binding-energy peak of 529.8 eV can be attributed to the Yb-O-Ta bonding. These low peak intensities are assigned to O-C (or O=C) bonds resulting from various species present in the organic carbon overlayer on top of the $YbTaO_4$ films. The peak intensities of $YbTaO_4$ and $Ta_2O_5$ components for the film annealed at 800 °C exhibited higher and lower, respectively, in the O 1 s signal compared with other temperatures. In addition, the O 1 s peak corresponding to $YbTaO_4$ for the sample annealed at 900 °C was a lower intensity than that at 800 °C. During high-temperature annealing, the more Ta or/and Yb atoms diffuse readily from the $YbTaO_4$ film to form a thicker silicate layer at the $YbTaO_4$–Si interface[14,15].

**Sensing and impedance characteristics of $YbTaO_4$ EIS sensors.** After the film material analyses, the sensing performance (pH sensitivity, hysteresis voltage and drift rate) of $YbTaO_4$ EIS sensors after RTA at three temperatures was investigated. The flatband voltage ($V_{FB}$) of an ISFET or EIS device can be expressed as:[27]

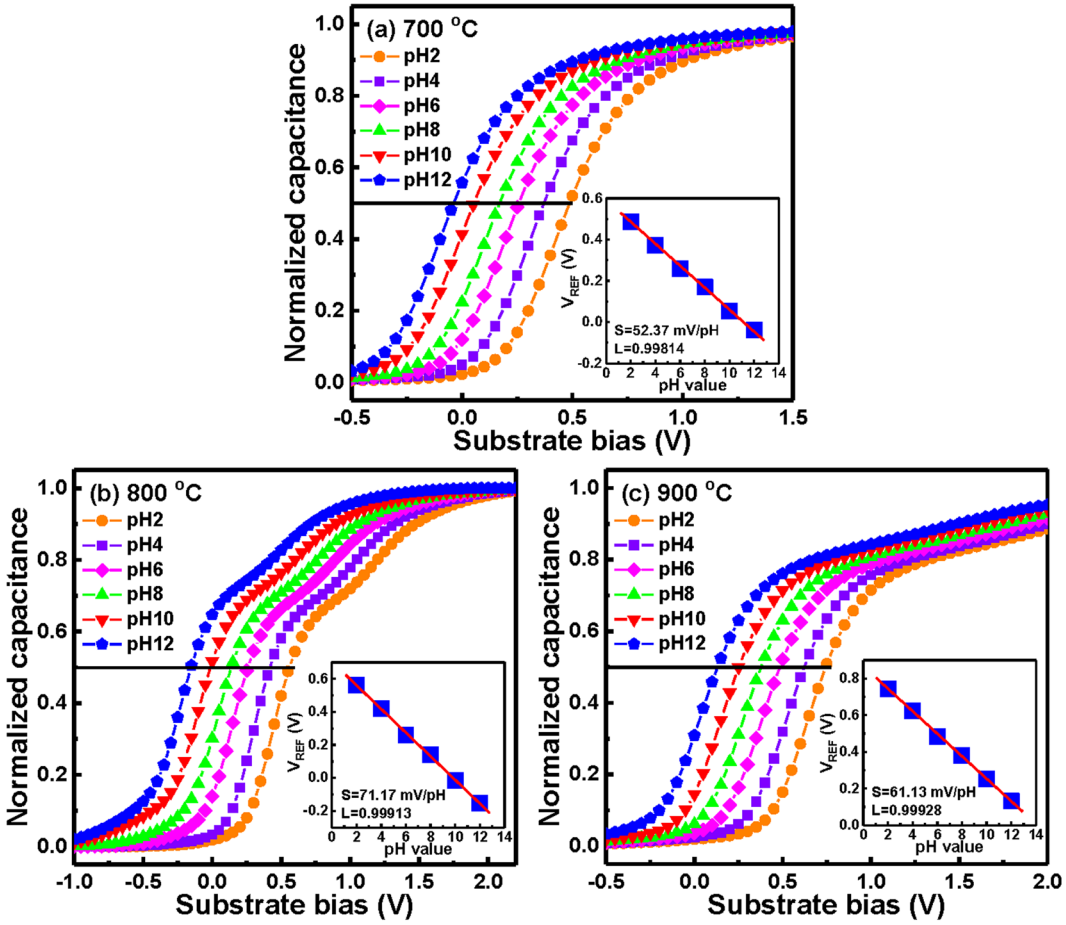


**Figure 4.** Responses of the *C*–*V* curves after inserting the $YbTaO_4$ sensors annealed at three RTA temperatures of (**a**) 700 °C, (**b**) 800 °C and (**c**) 900 °C, when submerged into solutions at values of pH ranging from 2 to 12. The insert in figure shows reference voltage of $YbTaO_4$ EIS sensors annealed at three RTA temperatures plotted as a function of pH at room temperature.

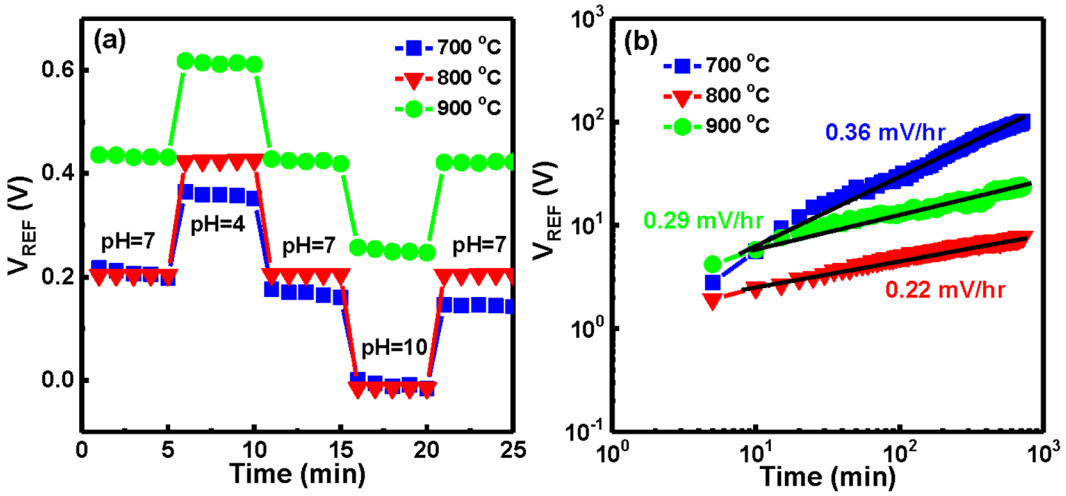


**Figure 5.** (**a**) Hysteresis curves of $YbTaO_4$ EIS sensors annealed at different RTA temperatures during the pH loop of 7→4→7→10→7. (**b**) Drift phenomena of $YbTaO_4$ EIS devices annealed at three RTA temperatures in a pH = 7 solution.

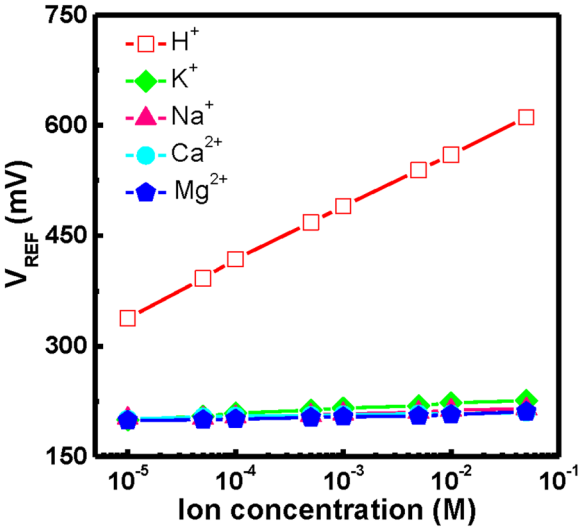


**Figure 6.** Reference voltage of $YbTaO_4$ EIS sensor annealed at 800 °C for different $H^+$, $K^+$, $Na^+$, $Ca^{2+}$, and $Mg^{2+}$ ion concentrations in pH 7.

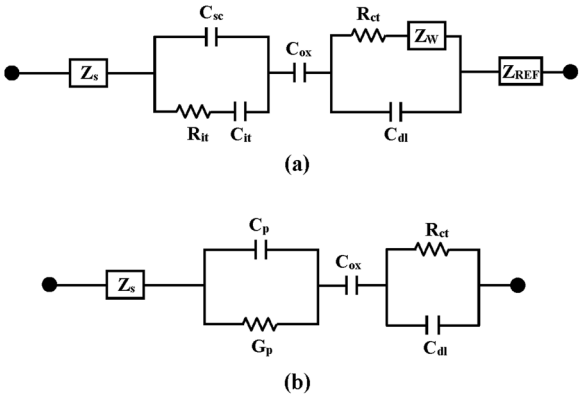


**Figure 7.** (**a**) Model of circuit elements present when the EIS device is immersed in a pH solution and (**b**) simplified equivalent circuit of an EIS device used in the study. Equivalent elements: $Z_s$, Si substrate impedance; $C_{sc}$, space charge capacitance; $C_{it}$, interface trap capacitance; $R_{it}$, interface trap resistance; $C_{ox}$, gate oxide capacitance; $C_{dl}$, double-layer capacitance; $R_{ct}$, charge transfer resistance; $Z_W$, Warburg impedance; $Z_{REF}$, reference impedance; $C_p$, frequency-dependent capacitance; $G_p$, frequency-dependent conductance.

$$V_{FB} = E_{ref} - \psi_0 + \chi^{sol} - \frac{\Phi_{Semi}}{q} - \frac{Q_{eff}}{C_{ox}} \tag{1}$$

where $E_{ref}$ is the reference electrode potential, $\psi_0$ is the surface potential, $\chi^{sol}$ is the surface dipole potential of the solution, $\Phi_{Semi}$ is the semiconductor work function, $q$ is the elementary charge, $Q_{eff}$ is the effective charge produced at the oxide-semiconductor interface and in the oxide by the different types of charges (e.g., interface trapped charge, fixed oxide charge, oxide trapped charge), and $C_{ox}$ is the gate oxide capacitance. Apart from $\psi_0$, all these terms are fixed values. This term causes an ISFET or EIS device responsive to the tested solution as a result of the polarization and formation of the potential barrier, which is related to the $H^+$ concentration. Therefore, an ISFET or EIS device can be sensitive to the solution pH. The potential of electrolyte-insulator interface corresponding to pH can be explained by using a combination of the site-binding model and the Gouy–Chapman–Stern theory[28]. The pH sensitivity of an ISFET device is derived from Bergveld[28] as follows:

$$\frac{\delta\psi_0}{\delta pH_s} = 2.303\alpha\frac{k_B T}{q}, \ \ with\ \alpha = \frac{1}{1 + \frac{2.303 k_B T C_{dif}}{q^2 \beta_{int}}} \tag{2}$$

where $\alpha$ represents a dimensionless sensitivity parameter which varies between 0 and 1, $C_{diff}$ indicates the differential capacitance of the electric double-layer, and $\beta_{int}$ stands for the intrinsic buffer capacity of the oxide

| Sensing membrane | Sensitivity (mV/pH) | Hysteresis (mV) | Drift rate (mV/h) |
|---|---|---|---|
| $Ta_2O_5$[9] | 55–58 | ~1 | <0.5 |
| $Al_2O_3$[10] | 53.23 | 4 | x |
| $ZrO_2$[11] | 60 | 5.26 | 0.68 |
| $HfO_2$[11] | 57.5 | 5.88 | 0.52 |
| $TiO_2$[34] | 61.44 | x | 8.94 |
| $SnO_2$[35] | 57.36 | 4.8 | 6.73 |
| $Yb_2Ti_2O_7$[22] | 61.11 | 1.6 | 0.25 |
| This work | 71.17 | <1 | 0.22 |

**Table 1.** Comparison of sensing performances (sensitivity, hysteresis voltage, and drift rate) of ISFET and EIS sensors fabricated with $Ta_2O_5$, $Al_2O_3$, $ZrO_2$, $HfO_2$, $TiO_2$, $SnO_2$, $Yb_2Ti_2O_7$, and $YbTaO_4$ sensing films.

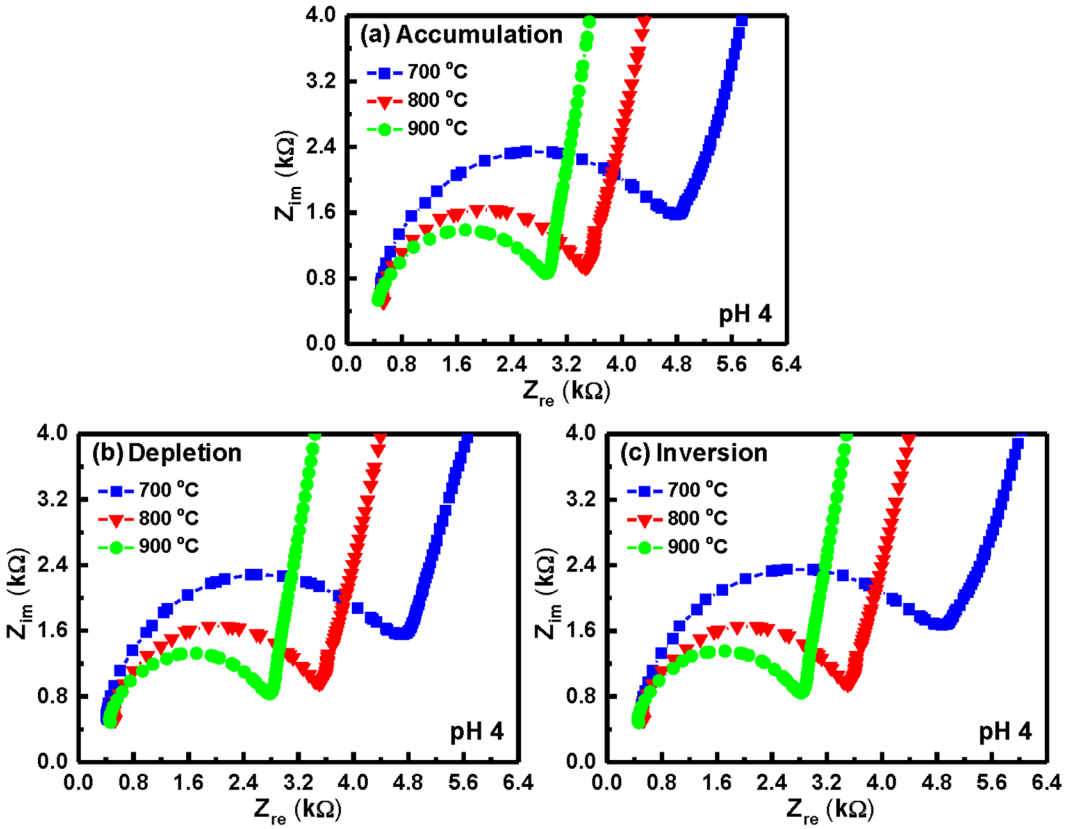


**Figure 8.** Nyquist diagrams ($Z_{im}$ vs. $Z_{re}$) of the $YbTaO_4$ EIS sensors annealed at three RTA temperatures and tested in the (**a**) accumulation, (**b**) depletion and (**c**) inversion regions, when immersed in a pH 4 solution.

surface. The above equation gives information that the $\beta_{int}$ and $C_{diff}$ are effectively influenced the pH sensitivity of an ISFET device. The $C_{diff}$ is obtained from the Gouy-Chapman-Stern model. In addition, the $\beta_{int}$ is related to the density of binding sites on the gate oxide. The higher the intrinsic buffer capacity $\beta_{int}$ is, the higher the pH sensitivity of the sensing film will achieve. The intrinsic buffer capacity is associated with the surface roughness and the material quality of the film. The change in the pH value of the electrolyte solution could give rise to a shift of the flatband voltage in the C-V curves.

In order to evaluate pH sensitivity of the $YbTaO_4$ EIS sensors after RTA at different temperatures, a set of C-V curves measured in a wide range of pH 2–12 was tested. Figure 4(a–c) show the normalized C-V curves of the $YbTaO_4$ EIS devices annealed at 700, 800 and 900 °C, respectively. For a p-type Si substrate, three zones were visible, namely the accumulation, inversion and depletion regions. The accumulation region is caused by a hole channel on the Si surface when a high positive voltage is applied to substrate electrode. In contrast, when a high negative voltage is applied to substrate electrode, an inversion layer of electrons is formed in the inversion region. The C-V measurements around the depletion region were conducted for electrolyte solutions with pH ranging from 2 to 12. It is evidence that the kinks of the EIS sensors annealed at 800 and 900 °C were found in the depletion region of the C-V curves, possibly indicating the presence of interface state at the oxide-substrate[29]. In an

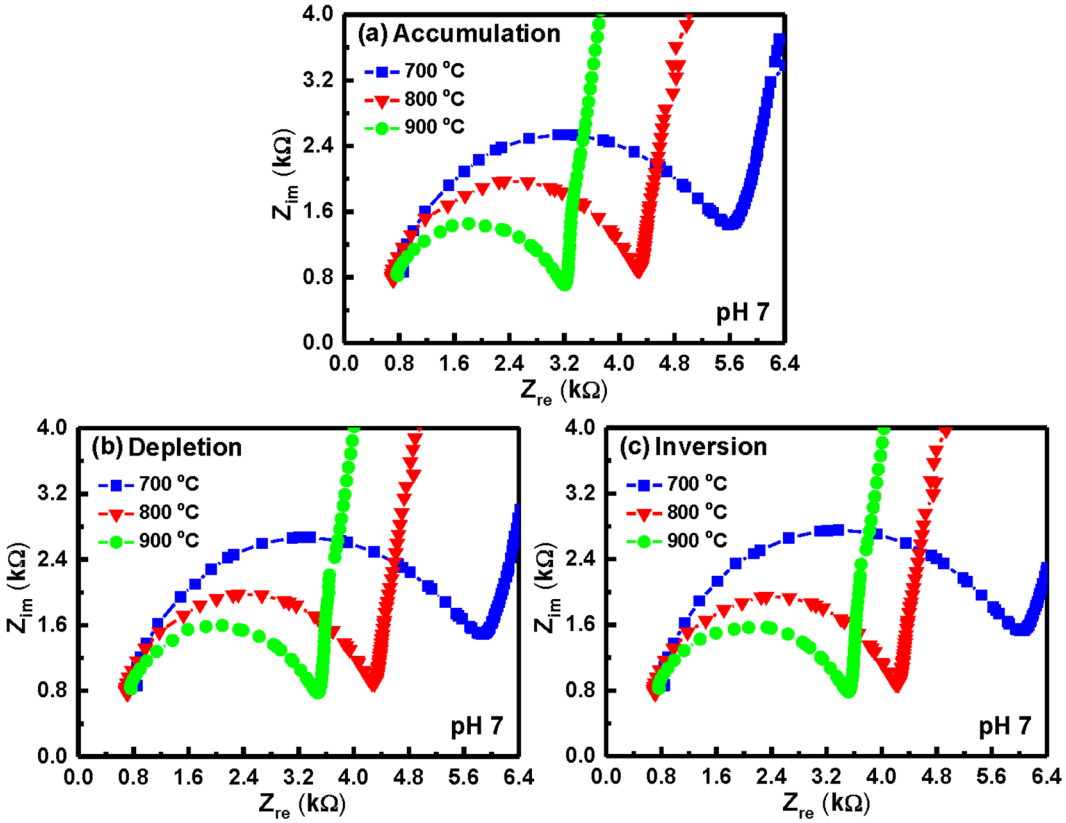


**Figure 9.** Nyquist diagrams ($Z_{im}$ vs. $Z_{re}$) of the $YbTaO_4$ EIS sensors annealed at three RTA temperatures and tested in the (**a**) accumulation, (**b**) depletion and (**c**) inversion regions, when immersed in a pH 7 solution.

ISFET operation, an adequate number of surface hydroxyl (OH) groups is essential on the gate oxide material for pH measurement at the Nernstian limit. The OH groups can protonate (positively charged, $OH_2^+$) or deprotonate (negatively charged, $O^-$)[27], which relies on the solution pH value. Therefore, the surface potential of the gate oxide changes, which can be measured via a capacitance variation of an EIS device. A negative shift of the reference voltage ($V_{REF}$) with increasing pH values of the investigated electrolyte solution reflects a more negatively charged gate oxide surface. The inset of Fig. 4(a–c) depicts the sensitivity and linearity of the $YbTaO_4$ EIS devices after RTA at 700, 800 and 900 °C, respectively. The $0.5C_{max}$ was set as the reference to extract the $V_{REF}$ versus the change of the pH value. The pH sensitivity and linearity of the C-V curves were achieved by linear regression. The $YbTaO_4$ EIS device annealed at 800 °C exhibited the highest sensitivity of $71.17 \pm 2.36$ mV/pH among these RTA temperatures ($52.37 \pm 3.25$ mV/pH for 700 °C and $61.13 \pm 2.26$ mV/pH for 900 °C). This result is mainly attributed to the film with a stoichiometric $YbTaO_4$ structure and a larger grain size of (−131) plane enhancing the pH sensitivity. Furthermore, the optimal RTA temperature in the oxygen ambient might improve the surface and interfacial material quality and increase the intrinsic buffer capacity ($\beta_{int}$). Furthermore, the pH sensitivity of the $YbTaO_4$ EIS sensor is higher than the theoretical Nernstian value of 59.4 mV/pH at 27 °C. This super-Nernstian value of our EIS sensor could be related to the mechanism of one transferred electron per 1.5 $H^+$ ion[30]. The decrease in pH sensitivity after RTA at 900 °C is the decrease of the surface state density of the OH groups[31].

Furthermore, the hysteresis curves of the $YbTaO_4$ EIS sensors with three RTA temperatures were shown in Fig. 5(a). The EIS sensors were submerged in the solutions of the pH loop of $7 \rightarrow 4 \rightarrow 7 \rightarrow 10 \rightarrow 7$. The hysteresis phenomenon might be due to the defects (e.g., oxygen vacancies, dangling bonds) of the film, these defects could react with the hydroxyl groups, thereby leading to hysteresis effect[32]. The $YbTaO_4$ EIS device after RTA at 800 °C had the lowest hysteresis voltage of $1 \pm 0.2$ mV among these annealing temperatures ($63 \pm 8.9$ mV for 700 °C and $11 \pm 2.8$ mV for 900 °C), suggesting that the optimal RTA temperature could effectively reduce the oxygen vacancies and dangling bonds. On the contrary, the EIS sensor annealed at 700 °C showed a relatively larger hysteresis voltage of 63 mV compared to other temperatures. This result could be attributed to a high number of defects in the $YbTaO_4$ film because these defects cannot be removed by the low annealing temperature. Figure 5(b) depicts the drift characteristics of the $YbTaO_4$ sensing films annealed at three RTA temperatures. Each of the EIS sensors was measured in a pH 7 buffer solution for a period of time. The change in the $V_{REF}$ can be expressed as $\Delta V_{REF} = V_{REF}(t) - V_{REF}(0)$. The slope of the drift characteristics indicates the drift rate of an EIS device. The drift effect can be interpreted by the hopping and/or trap-limited transport of water-related species[33], which the localized defects could interact with the tested solution, thus resulting in the gate voltage shift. Figure 5(b) demonstrates that the $YbTaO_4$ EIS sensor with the 800 °C had the lowest drift rate of $0.22 \pm 0.03$ mV/h, whereas the EIS device with the 700 °C featured the highest drift rate of $0.36 \pm 0.08$ mV/h. The lower drift rate may be due to the fact that the crystal defects could be eliminated by optimal RTA temperature in $O_2$ ambient, hence causing a

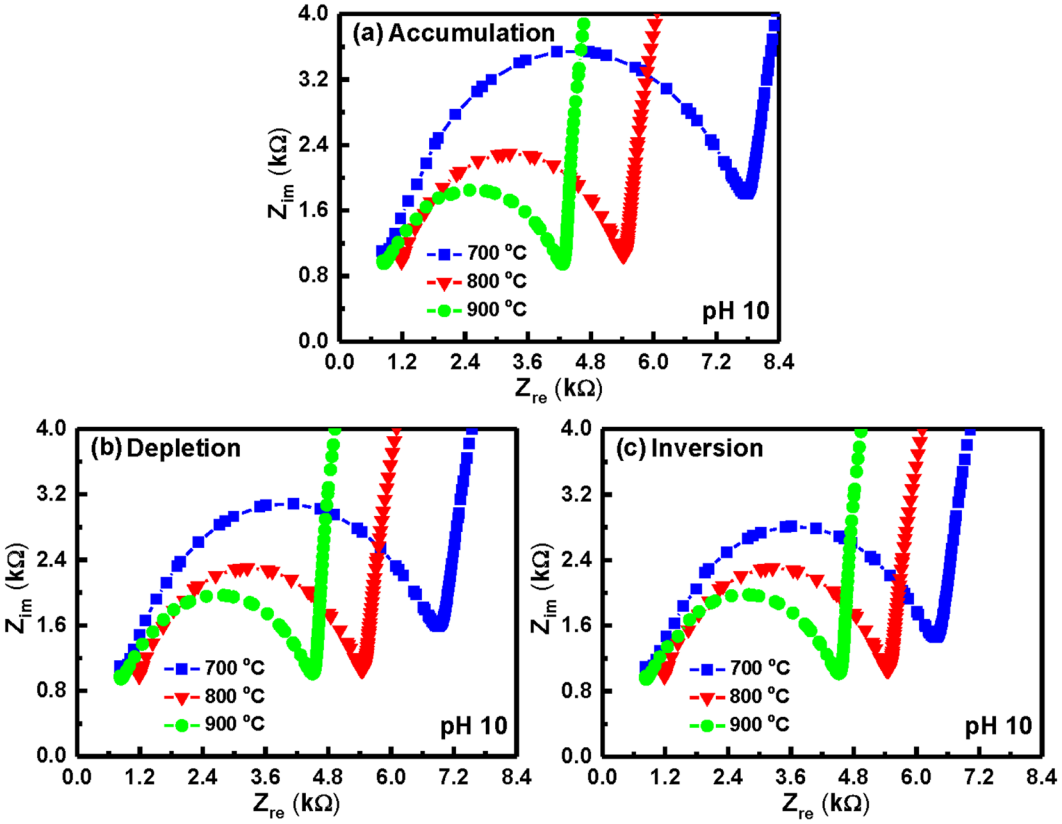


**Figure 10.** Nyquist diagrams ($Z_{im}$ vs. $Z_{re}$) of the $YbTaO_4$ EIS sensors annealed at three RTA temperatures and tested in the (**a**) accumulation, (**b**) depletion and (**c**) inversion regions, when immersed in a pH 10 solution.

lower capacitance of hydrated layer. In contrast, the higher drift rate could be contributed to the higher capacitance value of hydrated layer. In Table 1, the sensing performance of the $YbTiO_4$ membrane is compared with commonly used materials for EIS or ISFET-based sensors such as $Ta_2O_5$[9], $Al_2O_3$[10], $ZrO_2$[11], $HfO_2$[11], $TiO_2$[34], $SnO_2$[35], and $Yb_2Ti_2O_7$[22]. It is found that our $YbTiO_4$ membrane demonstrated a higher pH sensitivity (71.17 mV/pH), a smaller hysteresis voltage (<1 mV) and a lower drift rate (0.22 mV/h), relative to those of these materials.

Figure 6 shows the reference voltage of the $YbTiO_4$ EIS sensor annealed at 800 °C for various $H^+$, $K^+$, $Na^+$, $Ca^{2+}$, and $Mg^{2+}$ ion concentrations in pH 7. The response curves were measured in these ion concentrations ranging from $10^{-5}$ to 0.05 M. It is clear that the $YbTiO_4$ sensing membrane had high selectivity to $H^+$ ions and less selectivity to other ions, e.g. $K^+$, $Na^+$, $Ca^{2+}$, $Mg^{2+}$.

Electrochemical impedance spectroscopy is well established as a powerful tool for investigating the mechanisms of electrochemical reactions and measuring the dielectric and transport properties of materials. In addition, it can be successfully applied for the characterization of biosensing surfaces and/or in estimation of bioanalytical signals produced by biosensors. A small sinusoidal perturbation of potential measured is usually applied to an electrochemical device at different frequencies, thus monitoring the variation of electric current or voltage. Figure 7(a) depicts an equivalent circuit of the oxide surface/electrolyte solution interface in an EIS device. The Nyquist plots of the $YbTaO_4$ EIS devices annealed at three different RTA temperatures and tested at different solution pH values were presented in Figs 8–10. Each of the plots in all the $YbTaO_4$ EIS devices demonstrated a depressed semicircle portion at high frequency region and a slanted straight portion at low frequency region. The results indicate that the semicircle portion is related to charge transfer-limited process and the linear portion is associated with diffusion limited process or mass transfer process at oxide–electrolyte interface. At higher frequency end the intercept corresponds to the Si substrate impedance ($Z_S$) and at lower frequency corresponds to the sum of $Z_S$ and charge transfer resistance ($R_{ct}$). The value of $R_{ct}$ is a measure of electron transfer across the exposed area of the oxide surface. The conductance method, indicating the loss mechanism because of interface trap capture and emission of carriers, is generally employed to evaluate the density of interface trap states ($D_{it}$) in the depletion region for a MOSFET device[29]. If the capacitance has small losses in the oxide, a simplified equivalent circuit of an EIS sensor for conductance method was shown in Fig. 7(b). The measured conductance originates from the contribution of the interfacial trap states. According to the equivalent circuit of Fig. 7(b), two semicircle features may be observed in Nyquist plots: one is related to the sensing membrane response at higher frequencies, and the other is associated with the oxide–solution interface response at lower frequencies. Figures 8–10 demonstrate that single semicircles were observed in the frequency range 0.2 to 8 MHz for the $YbTaO_4$ EIS sensors with different RTA temperatures from 700 to 900 °C.

At pH 4, a semicircle diameter of the $YbTaO_4$ EIS sensors annealed at 700 °C exhibited larger compared with other temperatures, as shown in Fig. 8(a–c), suggesting that the EIS devices after RTA at higher temperature produce low bulk resistances. On the other hand, the diameter of the semicircle was almost the same value as the accumulation, depletion, and inversion regions. Figure 9(a–c) depict that the Nyquist plots of the $YbTaO_4$ EIS sensors after RTA at three temperatures were performed under three regions and then tested at pH 7. Here, a lower real impedance value (small semicircle) occurred at higher frequency, whereas a higher real impedance value (large semicircle) appeared at lower frequency. The impedance spectra ($Z_{im}$ vs. $Z_{re}$) of the $YbTaO_4$ EIS sensors annealed at the three temperatures and then tested at pH 10 under the three regions were shown in Fig. 10(a–c). The radius of the semicircles for these EIS sensors gradually decreased from ~3–3.6 to ~1.8–2.1 kΩ as the RTA temperature increased. Moreover, the radius of the semicircle in accumulation region was higher than those of depletion and inversion regions. Figures 8 and 10 demonstrate that the radius of the semicircles for the EIS sensors tested in the alkaline (pH 10) solution were higher than those in the acid (pH 4) solution. The size of $H_3O^+$ ions is larger than that of the $HO^-$ ions, thus leading to a low diffusion rate. Therefore, the bulk resistance of the EIS devices gradually increased from ~0.4 to ~1 kΩ as the pH value increased.

## Conclusions

The effect of RTA treatment on the structural, sensing and impedance characteristics of $YbTaO_4$ sensing films on Si substrates by means of reactive rf cosputtering was explored in the paper. Material analyses indicate that the $YbTaO_4$ sensing film after RTA at 800 °C could form a stoichiometric $YbTaO_4$ structure and increase the grain size of (−131) plane. The $YbTaO_4$ sensing film annealed at 800 °C exhibited a higher pH sensitivity of 71.17 mV/pH, a smaller hysteresis voltage of 1 mV and a lower drift rate of 0.22 mV/h, in comparison with other RTA temperatures. These results are attributed this RTA temperature to the reduction in the defects and the improvement in the material quality of the film and the interface of $YbTaO_4$-Si substrate. The semicircle radius of the Nyquist plot for $YbTaO_4$ EIS device performed under the accumulation region was larger than those under the depletion and inversion regions. Furthermore, the bulk resistance gradually decreased with increasing the RTA temperature, while it clearly increased with increasing the pH value. The $YbTaO_4$-based EIS sensor annealed at 800 °C is suitable for use in future medical and industrial biosensing applications.

## References


1. Bergveld, P. Development of an ion-sensitive solid-state device for neurophysiological measurements. *IEEE Trans. Biomed. Eng.* **17**, 70–71 (1970).
2. Bergveld, P. Thirty years of ISFETOLOGY what happened in the past 30 years and what may happen in the next 30 years. *Sen. Actuators B* **88**, 1–20 (2003).
3. Seo, H. I. *et al.* ISFET glucose sensor based on a new principle using the electrolysis of hydrogen peroxide. *Sen. Actuators B* **40**, 1–5 (1997).
4. Pijanowska, D. G. & Torbicz, W. pH-ISFET based urea biosensor. *Sen. Actuators B* **44**, 370–376 (1997).
5. Goncalves, D., Prazeres, D. M. F., Chu, V. & Conde, J. P. Detection of DNA and proteins using amorphous silicon ion-sensitive thin-film field effect transistors. *Biosen. Bioelectron.* **24**, 545–551 (2008).
6. Kalofonou, M., Georgiou, P., Ou, C. P. & Toumazou, C. An ISFET based translinear sensor for DNA methylation detection. *Sen. Actuators B* **161**, 156–162 (2012).
7. Kalofonou, M. & Toumazou, C. Semiconductor Technology for early detection of DNA methylation of cancer: From concept to practice. *Sen. Actuators B* **178**, 572–580 (2013).
8. Schoning, M. J. & Poghossian, A. Bio FEDs (field-effect devices): State-of-the-art and new directions. *Electroanalysis* **18**, 1893–1900 (2006).
9. Poghossian, A. & Schoning, M. J. Detecting both physical and (bio-) chemical parameters by means of ISFET devices. *Electroanalysis* **16**, 1863–1872 (2004).
10. Chou, J. C. & Weng, C. Y. Sensitivity and hysteresis effect in $Al_2O_3$ gate pH-ISFET. *Mater. Chem. Phys.* **71**, 120–124 (2001).
11. Dutta, J. C. & Thakur, H. R. Sensitivity determination of CNT-based ISFETs for different high- κ dielectric materials. *IEEE Sen. Lett.* **1**, 1500104 (2017).
12. Pogorelova, S. P. *et al.* Development of ion-sensitive field-effect transistor-based sensors for benzylphosphonic acids and thiophenols using molecularly imprinted $TiO_2$ films. *Anal. Chim. Acta* **504**, 113–122 (2004).
13. Goltz, G., Torres, J., Lajzerowicz, J. Jr. & Bomchil, G. Formation and characterization of tungsten silicide layers. *Thin Solid Films* **124**, 19–26 (1985).
14. Houssa, M. *High-k Gate Dielectrics* (Institute of Physics Publishing, 2004).
15. Scarel, G., Svane, A. & Fanciulli, M. *Rare Earth Oxide Thin Films: Growth, Characterization, and Applications* (ed. Fanciulli, M. & Scarel, G.) Ch. 1, 1–14 (Springer, 2007).
16. Leskela, M., Kukli, K. & Ritala, M. Rare-earth oxide thin films for gate dielectrics in microelectronics. *J. Alloys Comp.* **418**, 27–34 (2006).
17. Petit, L., Svane, A., Szotek, Z. & Temmerman, W. M. First principles study of rare-earth oxides. *Phys. Rev. B* **72**, 205118 (2005).
18. Ohmi, S. *et al.* Characterization of $La_2O_3$ and $Yb_2O_3$ thin films for high-k gate insulator application. *J. Electrochem. Soc.* **150**, F134–F140 (2003).
19. Zhao, Y., Toyama, M., Kita, K., Kyuno, K. & Toriumi, A. Moisture-absorption-induced permittivity deterioration and surface roughness enhancement of lanthanum oxide films on silicon. *Appl. Phys. Lett.* **88**, 072904 (2006).
20. Schroeder, T. *et al.* Titanium-added praseodymium silicate high-κ layers on Si(001). *Appl. Phys. Lett.* **87**, 022902 (2005).
21. van Dover, R. B. Amorphous lanthanide-doped $TiO_x$ dielectric films. *App. Phys. Lett.* **74**, 3041–3043 (1999).
22. Weng, W. H., Jhou, C. H., Xie, H. X. & Pan, T. M. Label-free detection of AR-V7 mRNA in prostate cancer using $Yb_2Ti_2O_7$–based electrolyte-insulator-semiconductor biosensors. *J. Electrochem. Soc.* **164**, B710–B717 (2016).
23. Tang, Y. *et al.* Hierarchical $TiO_2$ nanoflakes and nanoparticles hybrid structure for improved photocatalytic activity. *J. Phys. Chem. C* **116**, 2772–2780 (2012).
24. Mozhchil, R. N. *et al.* Electronic structure and thermal stability of rare earth metalloporphyrins based on ytterbium. *J. Surf. Investig.:X-Ra.* **11**, 517–522 (2017).
25. Teterin, Y. A. & Teterin, A. Y. Structure of X-ray photoelectron spectra of lanthanide compounds. *Russ. Chem. Rev.* **71**, 347–381 (2002).
26. Mannequin, C., Tsuruoka, T., Hasegawa, T. & Aonoa, M. Identification and roles of nonstoichiometric oxygen in amorphous $Ta_2O_5$ thin films deposited by electron beam and sputtering processes. *Appl. Surf. Sci.* **385**, 426–435 (2016).

27. Bergveld, P. & Sibbald, A. Comprehensive analytical chemistry: v.23: Analytical and biomedical applications of ion-selective field-effect transistors (Elsevier Science Publishing, 1988).
28. van Hal, R. E. G., Eijkel, J. C. T. & Bergveld, P. A novel description of ISFET sensitivity with the buffer capacity and double-layer capacitance as key parameters. *Sen. Actuators B* **24**, 201–205 (1995).
29. Nicollian, E. H. & Brews, J. R. *MOS Physics and Technology* (Wiley, 1982).
30. da Silva, G. M. *et al*. Development of low-cost metal oxide pH electrodes based on the polymeric precursor method. *Anal. Chim. Acta* **616**, 36–41 (2008).
31. Sneh, O. & George, S. M. Thermal stability of hydroxyl groups on a well-defined silica surface. *J. Phys. Chem.* **99**, 4639–4647 (1995).
32. Warren, W. L. *et al*. Microscopic nature of border traps in MOS oxides. *IEEE Trans. Nucl. Sci.* **41**, 1817–1827 (1994).
33. Jamasb, S., Collins, S. D. & Smith, R. L. A physical model for threshold voltage instability in $Si_3N_4$-gate $H^+$-sensitive FET's (pH-ISFET's). *IEEE Trans. Electron Devices* **45**, 1239–1245 (1998).
34. Yao, P. C., Chiang, J. L. & Lee, M. C. Application of sol–gel $TiO_2$ film for an extended-gate $H^+$ ion-sensitive field-effect transistor. *Solid State Sci.* **28**, 47–54 (2014).
35. Chou, J. C. & Wang, Y. F. Preparation and study on the drift and hysteresis properties of the tin oxide gate ISFET by the sol-gel method. *Sen. Actuators B* **86**, 58–62 (2002).

## Acknowledgements

The authors would like to thank the Ministry of Science and Technology of Taiwan for financially supporting this research under contract of MOST-106-2221-E-182-063.

## Author Contributions

T.-M.P. and J.-L.H. conceived experiments and data analysis and wrote manuscript. Y.S.H. assisted with experiment design and performed experiments and analyzed data. All authors discussed and commented on the manuscript.

## Additional Information

**Competing Interests:** The authors declare no competing interests.

**Publisher's note:** Springer Nature remains neutral with regard to jurisdictional claims in published maps and institutional affiliations.